Boltzmann- and non-Boltzmann-based thermometers in the first, second and third biological windows for the SrF2:Yb^{3+},Ho^{3+} nanocrystals under 980, 940 and 915 nm excitations

Linxuan Wang
National University of Defense Technology
Liang Li
National University of Defense Technology
Maohui Yuan (yuanmaohuino1@126.com)
National University of Defense Technology
Zining Yang
National University of Defense Technology
Kai Han
National University of Defense Technology
Hongyan Wang
National University of Defense Technology
Xiaojun Xu
National University of Defense Technology

Research Article

Keywords: NIR luminescence, non-thermally coupled energy levels, wide-range temperature sensing, tri-wavelength excitations

Posted Date: July 7th, 2022

DOI: https://doi.org/10.21203/rs.3.rs-1809509/v1

Abstract

Spectrally determination of temperature based on the lanthanide-doped nanocrystals (NCs) is a vital strategy to noninvasively measure the temperature in practical applications. Here, we synthesized a series of SrF_2:Yb^{3+}/Ho^{3+} NCs and simultaneously observed the efficient visible upconversion luminescence (UCL) and near-infrared (NIR) downconversion luminescence (DCL) under 980, 940 and 915 nm excitations. Subsequently, these NCs were further utilized for thermometers based on the Boltzmann (thermally-coupled levels, TCLs) and non-Boltzmann (non-thermally-coupled levels, NTCLs) of Ho^{3+} ions in the first (~ 650 nm), second (~ 1012 nm) and third (~ 2020) biological windows (BW-I, BW-II and BW-III) under tri-wavelength excitations. The thermometric parameters including the relative sensitivity (S_r) and temperature uncertainty (δT) are quantitatively determined on the I_{648}/I_{541} (BW-I), I_{1186}/I_{1012} (BW-II), and I_{1950}/I_{2020} (BW-III) transitions of Ho^{3+} ions in the temperature range of 303–573 K. Comparative experimental results demonstrated that the thermometer has superior performances.

1. Introduction

As a basic physical variable, the temperature is closely related to human life and practical activities. Traditional thermometers possess a relatively large size and need to be physically contacted with the measured object, which severely limits the accuracy of temperature detection and restricts the use of many fields such as biological issues, microelectronic circuits, and nanoscale applications [1]. Therefore, accurate, fast and noninvasive measurement of the temperature is of great significance to practical applications. Lanthanide-doped NCs based on FIR or LIR (luminescence intensity ratio) technology could be used as luminescent thermometers which have been extensively developed recently [2–5]. The reason is that lanthanide ions have abundant energy levels and their emissions are heavily dependent on the temperature. These lanthanide-doped luminescent thermometers show the advantages such as fast response, high spatial resolution, high sensitivity, wide adaptability, small error caused by power fluctuation of excitation light source and fluorescence loss [6–10].

Generally, the most present researches have focused on the thermally coupled energy levels (TCLs) of lanthanide ions which the ΔE is limited to 200–2000 cm^{-1} because this can ensure that the two levels are spectrally separated and not too far apart leading to the variation of thermalization is insignificantly observed [11–12]. Nevertheless, this additional requirement greatly restrains the utility of numerous NTCLs in lanthanide ions. Thus, the thermometers based on the NTCLs, which are no longer restricted to limitation of ΔE and can expand the detection wavelengths in a relatively wide range, can achieve relatively high S_r and low δT and further expand their applications [13–15]. Generally, the quantitative NTCLs model is established by using the Arrhenius equation which can break the restriction of the ΔE between the NTCLs and well predict the FIR and the accuracy of temperature measurement. As is well known, compared to the strong scattering and absorption effects of visible light in biological tissues, the so-called first (BW–Ⅰ: 650–950 nm), second (BW–Ⅱ: 950–1700 nm) and third (BW–Ⅲ: 1700–2500 nm) optically transparent BWs in the range of 650–2500 nm possess strong tissue penetration and has less

scattering, low absorption and weak spontaneous luminescence. Hence, the design of a thermometer, which can simultaneously measure the temperature in the BW–Ⅰ, BW–Ⅱ and BW–Ⅲ, has practical significance and needs in biological applications.

Up till now, many lanthanide ions have been used for temperature measurement, including Yb^{3+} and Ho^{3+} ions [16–19]. On the one hand, Yb^{3+} ions have a large absorption cross-section, no excited-state absorption, and a wide absorption spectrum (800–1100 nm) and emission spectrum (975–1200 nm) [20–21]. On the other hand, Ho^{3+} ions have abundant stepped energy levels and can effectively emit luminescence in a wide range from visible to NIR bands when co-doped with Yb^{3+} ions. Generally, the previously reported Ho^{3+}-based thermometers almost utilize the two TCLs of $^5F_4$ and $^5S_2$ centered at approximately 540 nm in the visible light based on the Boltzmann theory [22]. In addition, the traditional excitation laser wavelength is 980 nm which could lead to severe heat absorption by the water molecules, thus extremely restraining its application in biological issues. Actually, the Yb^{3+} ions have appreciable absorption capability in other excitation wavelengths (such as 915 nm) where the water absorption coefficient is relatively low. Therefore, exploring the thermometers under different wavelength excitations, especially covering the three biological windows, has very important value in biological applications. However, there still lacks the corresponding research on this aspect [23–25].

In this work, we synthesized a sequence of SrF_2:Yb^{3+}/Ho^{3+} (12/x mol%) NCs doped with different Ho^{3+} concentrations by hydrothermal method. We further investigated the doping Ho^{3+} concentrations dependent on both the UCL and DCL properties, as well as their mechanism of populations and transitions. Subsequently, the SrF_2:Yb^{3+}/Ho^{3+} (12/0.1 mol%) NCs with the stronger luminescence were selected to study the thermal effect under 980, 940 and 915 nm continuous-wave (CW) lasers with the same pumping power density of 110 W cm^{-2}. In addition, we innovatively investigated the temperature-dependent luminescence based on TCLs and NTCLs simultaneously under tri-wavelength excitations. The quantitative model we used successfully calculated the FIRs and determined the parameters of the thermometer in the first, second and third biological windows.

2. Experimental Sections

2.1 Synthesis of SrF_2:Yb^{3+}/Ho^{3+} NCs

The chemicals of $SrCl_2 \cdot 6H_2O$ (99.99%), $YbCl_3 \cdot 6H_2O$ (99.9%), $HoCl_3 \cdot 6H_2O$ (99.9%), $Na_3C_6H_5O_7$ (98%) and NH_4F (98%) were purchased from Aladdin (China). The synthesis procedure of NCs by a hydrothermal method is similar to our previous literature [26]. Take SrF_2:Yb^{3+}/Ho^{3+} (12/0.1 mol%) NCs as an example. Firstly, 1.758 mmol $SrCl_2$, 0.24 mmol $YbCl_3$ and 0.002 mmol $HoCl_3$ were dissolved in 10 mL deionized water and stirred for 1 hour. Secondly, 10 mL $Na_3C_6H_5O_7$ (1 M) and 20 mL NH_4F (1 M) aqueous solutions were added to the above mixed solutions and sequentially stirred for another 1 hour. Lastly, the mixtures were transferred into a 50 mL Teflon-lined autoclave and heated at 200°C for 8 hours. When the autoclave

was naturally cooled down to room temperature, the as-prepared SrF_2 NCs were collected by centrifugation at 6000 rpm for 4 minutes and washed with ethanol and deionized water several times. The final products were dried in an oven at 60 ºC for 12 hours and finally obtained the white powders for further use.

2.2 Characterization

The morphology and size of the as-prepared SrF_2 NCs were characterized by transmission electron microscopy (TEM). X-ray diffraction (XRD) patterns were measured using a powder diffractometer (Bruker D8 advance). The DCL and UCL spectra of SrF_2:Yb^{3+}/Ho^{3+} NCs were measured by a fluorescence spectrophotometer (Zolix Omni-l3072i) coupled with an R928 photomultiplier tube (PMT) for visible light detection and an InGaAs avalanche photodetector (ZPS-PN15) for NIR emissions collection. The excitation sources are semiconductor lasers with different wavelengths of 980, 940, and 915 nm. For temperature-dependent luminescence measurement, a temperature controller (RT 600, Shanghai Hotz Instrument Technology Co., Ltd) was used to change and control the temperature. At room temperature, the spectra in the wavelength range of 400–2200 nm was collected using the constructed experiment system. Then, the sample was heated by the temperature controller and the spectra was detected with a step of 25 K in the range of 303–573 K. Especially, we set the heating rate of the temperature controller to 12.5 K min^{-1} and kept the constant temperature for 12 minutes to ensure that the temperature of sample always reached the scheduled temperature during the spectrum acquisition process.

3. Results And Discussion

3.1 Structure characterization

Figure 1(a-e) shows the TEM images of SrF_2:Yb^{3+}/Ho^{3+}(12/x mol%) doped with different Ho^{3+} concentrations. The morphology of these NCs exhibits an ellipse or rectangle shape. Figure 1(f) demonstrates the average size of these synthesized NCs is about 50 nm. As shown in Figure 1(g), XRD patterns further prove that the diffraction peaks of the samples match the standard card of the SrF_2 phase (JCPDS No. 06-0262) well. Both the TEM and XRD characterizations reveal that the doping of small amounts of Yb^{3+} and Ho^{3+} ions has almost no effect on the lattice structure and morphology of the SrF_2 NCs.

3.2 DCL and UCL properties

Based on the practical photoluminescence results, we preliminarily determined the optimal doping concentration of Yb^{3+} is 12 mol% for obtaining the efficient DCL and UCL. Hence, the Yb^{3+} concentration is fixed at 12 mol% to conduct the photoluminescence experiments. Figure 2 shows the visible UCL and NIR DCL spectra of SrF_2:Yb^{3+}/Ho^{3+} (12/x mol%) NCs doped with different Ho^{3+} concentrations under the excitation of 980 nm laser. There are eight typical emission bands centered at 485, 541, 648, 750, 1012, 1186, 1950, and 2020 nm, which are ascribed to the transitions of $^5F_3 \rightarrow {}^5I_8$, $^5F_4(^5S_2) \rightarrow {}^5I_8$, $^5F_5 \rightarrow {}^5I_8$, $^5F_4$

$\rightarrow {}^5I_7$, ${}^5S_2 \rightarrow {}^5I_6$, ${}^5I_6 \rightarrow {}^5I_8$, ${}^5F_3 \rightarrow {}^5F_5$ and ${}^5I_7 \rightarrow {}^5I_8$ from Ho^{3+} ions, respectively. Obviously, the visible UCL and NIR DCL exhibit different variation trends as alters the doping Ho^{3+} ions. The visible UCL increases with the increase of Ho^{3+} concentrations within a low concentration range and reaches the maximum at 0.4 mol% Ho^{3+}, and then decreases sharply with the increase of Ho^{3+} ions again. Analysis of this phenomenon proves that concentration quenching plays an important role [27]. The increase of Ho^{3+} concentration promotes an increase in rare-earth-ion pair formation in the SrF_2 lattice which correspondingly reduces the distance between Ho^{3+} ions compared the Yb^{3+}-Ho^{3+} ions, thus facilitating the occurrence of cross-relaxation (CR) between the adjacent Ho^{3+} ions [28-29]. For the NIR DCL part, the 1012 and 2020 nm emission intensities gradually decrease with the increase of Ho^{3+} concentration, whereas the 1186 and 1950 nm emission intensities are opposite. We speculate that this is mainly due to the CR process of Ho^{3+} ions (CR1 and CR2 in Figure 3). The CR1 process of ${}^5I_7 + {}^5F_5 \rightarrow {}^5I_8 + {}^5F_3$ can promote the population of ${}^5F_3$ state and inhibit the population of ${}^5I_7$ state, which will enhance the 1950 nm emission and decrease the 2020 nm emission, respectively. Similarly, The CR2 process of ${}^5I_7 + {}^5S_2 \rightarrow {}^5I_6 + {}^5F_5$ enhances the population of ${}^5I_6$ state and simultaneously reduce the population of ${}^5S_2$ state, thus strengthening the 1186 nm emission and weakening the 1012 nm emission. Notably, the complex excited-state absorption (ESA) and energy transfer (ET) processes can also contribute to the above observed phenomenon.

Figure 3 illustrates the energy level diagram for Yb^{3+} and Ho^{3+} ions under 980 nm excitation, which also contains the ET, ESA, CR and non-radiative transition (NRT). Generally, Yb^{3+} ions can be populated through the ${}^2F_{7/2} \rightarrow {}^2F_{5/2}$ transition by directly absorbing 980 nm photon and then transfer the energy to adjacent Ho^{3+} ions through successive ET processes to populate the ${}^5I_6$, ${}^5F_5$ and ${}^5F_4$ states of Ho^{3+} [30–31]. Moreover, the ${}^5F_3$ state is populated by the CR (${}^5I_7 + {}^5F_5 \rightarrow {}^5I_8 + {}^5F_3$) process, followed generating the 485 nm (${}^5F_3 \rightarrow {}^5I_8$) and 1950 nm (${}^5F_3 \rightarrow {}^5F_5$) emissions. Subsequently, the electrons in the ${}^5F_4$ state will transition to the ${}^5I_8$ and ${}^5I_7$ states, thereby emitting the 541 nm green light and 750 nm red emission, respectively. Simultaneously, partial electrons in the ${}^5F_4$ state will populate to the ${}^5S_2$ state by the NRT process, subsequently transition to the ${}^5I_6$ generating NIR emission at 1012 nm. Similarly, the electrons in the ${}^5F_5$ state will transition to the ${}^5I_8$ state, thereby emitting the 648 nm emission. Additionally, the transitions from the ${}^5I_6$ and ${}^5I_7$ states to ${}^5I_8$ state produce the 1186 nm and 2020 nm NIR emissions, respectively.

Notably, except excited by the 980 nm, the Yb^{3+} ions can also be excited at 940 and 915 nm lasers and then transfer energy to Ho^{3+} ions by ET process [32-33]. To further explore the influence of different excitation sources on the emission spectra for the SrF_2:Yb^{3+}/Ho^{3+} NCs, we further investigate the photoluminescence properties of SrF_2:Yb^{3+}/Ho^{3+} (12/0.1 mol%) NCs under the 980, 940 and 915 nm excitations with the same pumping power density (11 W cm^{-2}), as shown in Figure 4. The results show that emission efficiency under 980 nm excitation is the highest compared with the 915 and 940 nm

excitations, indicating that the largest absorption cross-section at 980 nm and lowest absorption cross-section at 940 and 915 nm. Under the same pumping power density, the intensity of visible emissions under 980 nm excitation is almost 40 times than that under 940 nm excitation and 80 times than 915 nm excitation, while the NIR light is almost 4.5 times than that under 940 nm excitation and 9 times than that 915 nm excitation.

Figure 5(a) displays the thermal images of SrF_2:Yb^{3+}/Ho^{3+} (12/0.1 mol%) NCs dispersed in ethanol solutions under the 980, 940 and 915 nm laser illustration with a step of 240 s. The excitation power density is 110 W cm^{-1}. Over the 1440 seconds of the testing process, the temperature gradually rises while manifesting different magnitudes for different excitation wavelengths. Figure 5(b) further depicts the plot of temperature changes as a function of the heating times. During the heating time, the maximum temperature increases up to 38.5°C and 41.8°C under 915 and 980 nm excitations, respectively. In contrast, the temperature merely elevates from an initial 23.6°C to the final 27.4°C under 940 nm excitation. Obviously, the 940 nm laser-induced heating effect is unconspicuous compared to the 915 and 980 nm lasers. Therefore, under the excitations of 940 nm and 915 nm, the design of a higher sensitivity thermometer has more significant significance in the biological and medical fields.

3.3 Ratiometric temperature sensing

Having obtained the efficient visible UCL and NIR DCL simultaneously under the excitation of 980, 940 and 915 nm lasers, here we continue to investigate the ratiometric temperature sensing performances. Figure 6 displays the temperature-dependent spectra of SrF_2:Yb^{3+}/Ho^{3+} (12/0.1 mol%) NCs under the excitation of 980, 940 nm and 915 nm in the range of 303–573 K. Both the visible and NIR emissions are decreasing with the increasing of temperature. However, the visible UCL thermally quenches more obviously than the NIR DCL. Under the 980 nm excitation, the intensity of visible 541 nm UCL at room temperature (303 K) is about 95 times than that at the highest temperature of 573 K, while red UCL (648 nm) decreases about 16 times from the 303 K to 573 K, as shown in Fig. 6(a). On the contrary, the NIR DCL remains slightly changes when the temperature varies from room temperature to 573 K, which possesses a relative highly thermal stability compared with the visible UCL. Particularly, the NIR DCL remains almost unchanged under the 915 nm excitation.

The temperature-dependent spectra ranging from the BW-I, BW-II and BW-III significantly demonstrates that it can be used for detecting the temperature in a wide range. Considering the actual energy levels of Ho^{3+} ions, especially both TCLs and NTCLs emissions, we choose different methods to analyze and calculate the performances of the Boltzmann-based and non-Boltzmann-based thermometers based on the TCLs or NTCLs. Traditional FIR technology measures the thermal dependence of FIR based on TCLs, which can be defined as:

$$FIR_B = \frac{N_1}{N_2} = \frac{I_1}{I_2} = A\exp(-\frac{\Delta E}{KT})$$

1

Where, N and I represent the populations of the corresponding energy levels and fluorescence intensity, respectively. A is the constant that depends on the experimental system, T is the absolute temperature and K is the Boltzmann constant.

Arrhenius equation is undoubtedly a good method to analyze the mechanism of temperature sensing behavior when using the NTCLs method, which can be expressed as follows [34]:

$$I(T) = I_0/(1 + B\mathrm{e}^{(-E_a/KT)})$$

2

Where, I_0 is the UCL intensity of the measured NCs at room temperature (T_0), I(T) is the UCL intensity at temperature T, B is the constant and E_a is the quenching activation energy. The definition of T and K is the same to Eq. (1).

Therefore, the FIR based on NTCLs can be modified as follows [35–36]:

$$FIR_{N-B} = \frac{I_1(T)}{I_2(T)} = \frac{I_{0,1}}{I_{0,2}}\frac{1 + B_2\exp(-E_2/KT)}{1 + B_1\exp(-E_1/KT)} \approx \alpha + \beta\exp(-\frac{\Delta E_a}{KT})$$

3

Where, I_1(T) and I_2(T) represent the UCL intensity of the two corresponding UCL emissions at temperature T, respectively. α and β are constants that are dependent on I_0 and I(T). E_1 and E_2 are the corresponding quenching activation energy. $\Delta E_a$is a parameter associated with E_1 and E_2.

Figure 7 shows the FIR ratios of I_{648}/I_{541}, I_{1186}/I_{1012} and I_{1950}/I_{2020} as a function of the external temperature under tri-wavelength excitations. To ensure the accuracy of experimental data, we fitted the FIR ratios using the Gaussian fitting based on the integrated areas of each UCL peak. As a result, the values of FIR increase with the increase of temperature. Among them, the FIR of I_{648}/I_{541} is fitted with equation (1), and the FIR of I_{1186}/I_{1012} and I_{1950}/I_{2020} are fitted with equation (3). All the fitting R^2 values of curves are greater than 99.0%, indicating that the rationality of the FIR model is based on the TCLs and NTCLs.

To better evaluate the capability of a thermometer, the S_R is used to represent the relative sensitivity of the thermometer, which is defined as follows [37–38]:

$$S_{R,B} = \frac{1}{FIR}\left|\frac{\partial FIR}{\partial T}\right| = \frac{\Delta E}{KT^2}$$

4

$$S_{R,N-B} = \frac{1}{FIR}\left|\frac{\partial FIR}{\partial T}\right| = \frac{\Delta E_a}{KT^2}\frac{\beta\exp(-\Delta E_a/KT)}{\alpha+\beta\exp(-\Delta E_a/KT)} \quad (5)$$

Equations (4) and (5) are the expressions S_R based on TCLs and NTCLs, respectively.

Figure 8 displays the relative sensitivity of different FIRs based on TCLs and NTCLs dependent on the temperature. In general, for all the UCL emission ratios, the S_R under 980 nm excitation is the highest, and the S_R under 940 nm excitation is the lowest. Particularly, the maximum S_R of I_{648}/I_{541} based on TCLs reaches 0.94 % K^{-1}, 0.57 % K^{-1} and 0.85 % K^{-1} at the room temperature of 303 K under tri-wavelength excitations, and the value S_R decreases gradually with the increase of temperature which is consistent with that described in Equation (4). It is interesting to note that the maximum S_R of I_{1186}/I_{1012} and I_{1950}/I_{2020} based on NTCLs uner 980 nm ecitation reachs 0.45 % K^{-1} and 0.40 % K^{-1} at the same temperature of 523 K. And the maximum S_R of I_{1186}/I_{1012} attains 0.23 % K^{-1} at 303 K whereas the maximum S_R of I_{1950}/I_{2020} reaches 0.17 % K^{-1} at 398 K under 940 nm excitation. This is because the amplitude of fluorescence intensity varies with temperature under different excitation soures discrepantl, as shown in Figure 6. In particular, the variation of NIR fluorescence intensity uder excitation of 940 and 915 nm is significantly smaller than hat under excitation of 980 nm, which leads to a higher relative sensitivity under 980 nm excitation.

For comparison, Table 1 summarizes the performances of our determined thermometers and compared them to the previously reported thermometers related to Ho^{3+} ions. The relatively higher performance can be achieved in the range of 303–573 K for FIRs of I_{648}/I_{541}, I_{1186}/I_{1012} and I_{1950}/I_{2020} in our experiment compared to the previous Ho^{3+}-doped thermometers.

Table 1

The parameters of λ_{ex}, λ_{em}, maximum S_R, temperature range of the Ho^{3+}-doped materials.

Samples	λ_{ex} (nm)	λ_{em} (nm)	NTCLs or TCLs	Temperature range (K)	S_R(%•K^{-1})	References
$NaYF_4$: Ho^{3+}	447	542, 645	TCLs	113–473	0.93 (302 K)	[12]
$BaTiO_3$:Ho^{3+},Yb^{3+}	980	539, 547	TCLs	305–515	0.34 (305 K)	[16]
$LiYF_4$: Yb^{3+}, Ho^{3+}	976	655, 546	TCLs	100–500	0.0129 (156 K)	[30]
$BiPO_4$:Yb^{3+},Ho^{3+}	980	652, 657	TCLs	313–573	0.079 (333 K)	[31]
NBT:Ho^{3+},Yb^{3+}	980	546, 757	TCLs	93–300	0.29 (93 K)	[36]
$LiYb(WO_4)_2$:Yb^{3+},Ho^{3+}	980	541, 663	TCLs	298–573	0.7 (300 K)	[39]
$(K_{0.5}Na_{0.5})NbO_3$:Ho^{3+}	980	526, 552	TCLs	300–650	0.75 (430 K)	[40]
SrF_2:Yb^{3+},Ho^{3+}	980	648, 541	TCLs	303–573	0.94 (303 K)	This work
		1186, 1012	NTCLs	303–573	0.45 (523 K)	This work
		1950, 2020	NTCLs	303–573	0.40 (523 K)	This work
	940	648, 541	TCLs	303–573	0.57 (303 K)	This work
		1186, 1012	NTCLs	303–573	0.23 (303 K)	This work
		1950, 2020	NTCLs	303–573	0.17 (398 K)	This work
	915	648, 541	TCLs	303–573	0.85 (303 K)	This work
		1186, 1012	NTCLs	303–573	0.15 (303 K)	This work
		1950, 2020	NTCLs	303–573	0.24 (303 K)	This work

In addition to S_R, the temperature uncertainty of δT is a very significant parameter used to evaluate the performance of a thermometer, which is defined as [41]:

$$\delta T = \frac{1}{S_R}\frac{\delta \Delta}{\Delta} \times 100\%$$

6

Where, Δ is the average of measured FIR values in the experiment and $\delta\Delta$ is the uncertainty of the calculated FIR. Based on the equation (6), we have calculated the temperature uncertainty of δT for the I_{1950}/I_{2020}. We have obtained the $\delta T <$ 1.25 K under 980 nm excitation while $\delta T <$ 0.96 K under 915 nm excitation in the temperature range of 303–573 K. In addition, Figure 9 shows the good repeatability of the temperature-dependent FIR for the NIR bands measured in several heating and colling circles. The results indicate that the thermometer based on NTCLs of Ho^{3+} has relatively high sensitivity and low temperature uncertainty.

4. Conclusions

In conclusion, SrF_2:Yb^{3+}/Ho^{3+} (12/x mol%) NCs with an average size of ~ 50 nm were synthesized through the hydrothermal method and characterized by TEM and XRD. Both the efficient NIR DCL and visible UCL are observed under 980, 940 and 915 nm excitations. The doping Ho^{3+} concentrations dependent on the UCL and DCL, as well as their mechanism of population processes and emission transitions are also discussed. Subsequently, the SrF_2:Yb^{3+}/Ho^{3+} (12/0.1 mol%) NCs exhibited the most intense NIR DCL and visible UCL. Then, these NCs were selected to achieve the Boltzmann- and non-Boltzmann-based thermometers under 980, 940 and 915 nm excitations. The obtained maximum S_R of I_{648}/I_{541} based on TCLs is 0.94 $\%K^{-1}$ at 303 K, as well as the 0.45 $\%K^{-1}$ for I_{1186}/I_{1012} and 0.40 $\%K^{-1}$ for I_{1950}/I_{2020} at 523 K based on NTCLs under 980 nm excitation. The results reveal that these NCs can be applied in biological issues to measure the temperature under different laser wavelength excitations and wide emission bands centered in the first, second and third biological windows.

Abbreviations

NCs: nanocrystals; UCL: Upconversion luminescence; DCL: downconversion luminescence; NIR: near-infrared; TCLs: thermally-coupled levels; NTCLs: non-thermally-coupled levels; BW-I: first biological windows; BW-II: second biological windows; BW-III: third biological windows; CW: Continuous-wave; TEM: Transmission electron microscopy; XRD: X-ray diffraction; PMT: photomultiplier tube; CR: Cross-relaxation; ESA: excited-state absorption; ET: energy transfer; NRT: non-radiative transition.

Declarations

Ethics approval and consent to participate

Not applicable.

Consent for publication

Not applicable.

Availability of Data and Material

The datasets used and/or analysed during the current study are available from the corresponding author on reasonable request.

Competing Interests

The authors declare that they have no competing interests.

Funding

Not applicable.

Authors' Contributions

LW and MY contributed to the design of this research. LW and MY carried out the experiments. LW, KH and LL contributed to the data analysis. LW and HW provided the optical spectrum test and measurement. LW and MY wrote the draft of the manuscript. HW and XX revised and finalized the manuscript. All authors have read and approved the final manuscript.

Acknowledgments

Not applicable.

References

1. Van Swieten TP, Yu DC, Yu T, Vonk SJW, Suta M, Zhang QY, Meijerink A, Rabouw FT (2021) A Ho^{3+}-based luminescent thermometer for sensitive sensing over a wide temperature range. Adv Opt Mater 9:2001518
2. Li D, Mo J, Wang C, Liu W, Ge H, Han D, Hao A, Chai B, She J (2020) Screen printing of upconversion $NaYF_4$:Yb^{3+}/Eu^{3+} with Li^+ doped for anti-counterfeiting application. Chin Opt Lett 18:110501
3. Yu B, Zheng B, Xia H, Wang J, Song H, Chen B (2021) Tunable emission and temperature sensing performance in novel oxyfluoride borosilicate glass ceramics containing Eu^{3+}/Tb^{3+}:KY_3F_{10} nanocrystals. Ceram Int 47:9668–9678
4. Yang X, Wang L, Wang R, Yang Z, Song C, Yuan M, Han K, Lan S, Wang H, Xu X (2021) Achieving tunable multicolor display and sensitive temperature sensing in self-sensitization of erbium-doped CaF_2 nanocrystals under 808, 980 and 1532 nm irradiation. Opt Mater Express 11:2514–2527
5. Periša J, Đorđević V, Ristić Z, Medić M, Kuzman S, Antić Ž, Dramićanin MD (2022) Highly sensitive temperature reading from intensity ratio of Eu^{3+} and Mn^{4+} emissions in $Y_3Al_5O_{12}$ nanocrystals. Mater Res Bull 149:111708

6. Gao G, Busko D, Kauffmann-Weiss S, Turshatov A, Howard IA, Richards BS (2018) Wide-range non-contact fluorescence intensity ratio thermometer based on Yb^{3+}/Nd^{3+} co-doped La_2O_3 microcrystals operating from 290 to 1230 K. J Mater Chem C 6:4163–4170
7. Zhong J, Chen D, Peng Y, Lu Y, Chen X, Li X, Ji Z (2018) A review on nanostructured glass ceramics for promising application in optical thermometry. J Alloy Compd 763:34–48
8. Dong H, Du S, Zheng X, Lyu GM, Sun L, Li L, Zhang P, Zhang C, Yan C (2015) Lanthanide nanoparticles: from design toward bioimaging and therapy. Chem Rev 115:10725–10815
9. Mancic L, Djukic-Vukovic A, Dinic I, Nikolic MG, Rabasovic MD, Krmpot AJ, Costa AMLM, Trisic D, Lazarevic M, Mojovic L, Milosevic O (2018) NIR photo-driven upconversion in $NaYF_4$:Yb,Er/PLGA particles for in vitro bioimaging of cancer cells. Mat Sci Eng C 91:597–605
10. Kıbrıslı O, Erol E, Vahedigharehchopogh N, Yousef ES, Çelikbilek-Ersundu M, Ersundu AE (2020) Noninvasive optical temperature sensing behavior of Ho^{3+} and Ho^{3+}/Er^{3+} doped tellurite glasses through up and down-converted Emissions. Sensor Actuat A 315:112321.
11. Cheng Y, Gao Y, Lin H, Huang F, Wang Y (2018) Strategy design for ratiometric luminescence thermometry: circumventing the limitation of thermally coupled levels. J Mater Chem C 6:7462–7478
12. Xu H, Yang Y, Lu L, Yang Y, Zhang Z, Zhao C, Zhang F, Fan Y (2022) Orthogonal multiplexed NIR-II imaging with excitation-selective lanthanide-based nanoparticles. Anal Chem 94:3661–3668
13. Wang C, Jin Y, Zhang R, Yao Q, Hu Y (2022) A review and outlook of ratiometric optical thermometer based on thermally coupled levels and non-thermally coupled levels. J Alloy Compd 894:162494
14. Liu S, Cui J, Jia J, Fu J, You W, Zeng Q, Yang Y, Ye X (2019) High sensitive $Ln^{3+}/Tm^{3+}/Yb^{3+}$ (Ln^{3+} = Ho^{3+}, Er^{3+}) tri-doped $Ba_3Y_4O_9$ upconverting optical thermometric materials based on diverse thermal response from non-thermally coupled energy levels. Ceram Int 45:1–10
15. Ran WG, Noh HM, Park SH, Lee BR, Kim JH, Jeong JH, Shi JS (2019) Application of thermally coupled energy levels in Er^{3+} doped $CdMoO_4$ phosphors: Enhanced solid-state lighting and non-contact thermometry. Mater Res Bull 117:63–71
16. Singh P, Yadav RS, Singh P, Rai SB (2021) Upconversion and downshifting emissions of Ho^{3+}-Yb^{3+} co-doped $ATiO_3$ perovskite phosphors with temperature sensing properties in Ho^{3+}-Yb^{3+} co-doped $BaTiO_3$ J Alloy Compd 855:157452
17. Marciniak L, Elzbieciak-Piecka K, Kniec K, Bednarkiewicz A (2020) Assessing thermometric performance of Sr_2CeO_4 and Sr_2CeO_4:Ln^{3+} (Ln^{3+} = Sm^{3+}, $Ho^{3+,}$ Nd^{3+}, Yb^{3+}) nanocrystals in spectral and temporal domain. Chem Eng J 388:124347
18. Pominova D, Proydakova V, Romanishkin I, Ryabova A, Kuznetsov S, Uvarov O, Fedorov P, Loschenov V (2020) Temperature sensing in the short-wave infrared spectral region using core-shell $NaGdF_4$:Yb^{3+}, Ho^{3+}, Er^{3+}@$NaYF_4$ Nanomaterials 10:1992
19. Pushpendra, Kunchala RK, Kalia R, Naidu BS (2020) Upconversion luminescence properties of $NaBi(MoO_4)_2$:Ln^{3+}, Yb^{3+} (Ln = Er, Ho) nanomaterials synthesized at room temperature. Ceram Int

46:18614–18622

20. Wu Q, Xu Z, Wageh S, Al-Ghamdi A, Zhao S (2021) The dynamic variation of upconversion luminescence dependent on shell Yb^{3+} contents in $NaYF_4$: Yb^{3+},Tm^{3+}@$NaYF_4$: Yb^{3+},Er^{3+} J Alloy Compd 891:162067
21. Wei W, Zhang Y, Chen R, Goggi J, Ren N, Huang L, Bhakoo KK, Sun HD, Tan TTY (2014) Cross relaxation induced pure red upconversion in activator- and sensitizer-rich lanthanide nanoparticles. Chem Mater 26:5183–5186
22. Li Z, Lin L, Feng Z, Huang L, Wang Z, Zheng Z (2021) Wide-range temperature sensing of $NaYF_4$: Ho^{3+} nanoparticles by multi-emissions in dual spectral ranges. J Lumin 232:117873
23. Fan Q, Zhang G, Peng B (2021) Tumor imaging of a novel Ho^{3+}-based biocompatible NIR fluorescent fluoride nanoparticle. J Lumin 235:118007
24. Leal JJ, Rodríguez E, Nava-Dino CG, Maldonado-Orozco MC, Gaxiola F, NarroGarcía R (2021) Effect of Ho^{3+} concentration on the luminescent and thermal stability of tellurite glasses. Mater Res Bull 144:111483
25. Gao W, Wang B, Han Q, Gao L, Wang Z, Sun Z, Zhang B, Dong J (2020) Multicolor upconversion emission of Ho^{3+} in single $NaYF_4$ J Alloy Compd 818:152934
26. Wang L, Yang X, Yuan M, Yang Z, Han K, Wang H, Xu X (2022) Determination of near-infrared downconversion emission of Yb^{3+} and optical temperature sensing performances in Nd^{3+}-sensitized SrF_2 Opt Mater 123:0925–3467
27. Yu X, Zhao T, Wang T, Bao W, Zhang H, Su C (2021) Up-conversion luminescence properties of Ho^{3+}-Yb^{3+} co-doped transparent glass ceramics containing $Y_2Ti_2O_7$. J Non-Cryst Solids 574:121163
28. Karthickraja D, Kumar GA, Sardar DK, Karthi S, Dannangoda GC, Martirosyan KS, Prasath M, Gowri M, Girija EK (2021) Fabrication of Nd^{3+} and Yb^{3+} doped NIR emitting nano fluorescent probe: A candidate for bioimaging applications. Mat Sci Eng C 125:112095
29. Cao C, Xue M, Zhu X, Yang P, Feng W, Li F (2017) Energy transfer highway in Nd^{3+}-sensitized nanoparticles for efficient near-infrared bioimaging. ACS Appl Mater Interfaces 9:18540–18548
30. Li W, Hu L, Chen W, Sun S, Guzik M, Boulon G (2021) The effect of temperature on green and red upconversion emissions of $LiYF_4$:20Yb^{3+}, 1Ho^{3+} and its application for temperature sensing. J Alloy Compd 866:158813
31. Wan N, Fu Z, Wei Y, Sheng T (2019) Investigation for the upconversion luminescence and temperature sensing mechanism based on $BiPO_4$: Yb^{3+}, RE^{3+} (RE^{3+} = Ho^{3+}, Er^{3+} and Tm^{3+}). J Alloy Compd 772:371–380
32. Sun Y, Yang Z, Xie C, Jiang Z (2012) Preparation and characteristics of core–shell structure $Y_3Al_5O_{12}$:Yb^{3+}@SiO_2 J Alloy Compd 528:1–9.
33. Zhan Q, Qian J, Liang H, Somesfalean G, Wang D, He S, Zhang Z, Andersson-Engels S (2011) Using 915 nm laser excited Tm^{3+}/Er^{3+}/Ho^{3+}-doped $NaYbF_4$ upconversion nanoparticles for in vitro and

deeper in vivo bioimaging without overheating irradiation. ACS Nano 5:3744–3757

34. Rodríguez-Díaz JM, Santos-Martín MT (2009) Study of the best designs for modifications of the Arrhenius equation. Chemom Intell Lab Syst 95:199–208
35. Li P, Jia M, Liu G, Zhang A, Sun Z, Fu Z (2019) Investigation on the fluorescence intensity ratio sensing thermometry based on nonthermally coupled levels. ACS Appl Bio Mater 2:1732–1739
36. Lu Z, Li K, Wang J, Luo L (2021) Photochromic and temperature sensing properties of Ho^{3+}-Yb^{3+} codoped $Bi_{495-x}Na_{0.5}TiO_3$ ceramics. Opt Mater 111:110718
37. Ćirić A, Stojadinović S, Dramićanin MD (2020) Luminescence temperature sensing using thin-films of undoped Gd_2O_3 and doped with Ho^{3+}, Eu^{3+} and Er^{3+} prepared by plasma electrolytic oxidation. Ceram Int 46:23223–23231
38. Kaczmarek AM, Suta M, Rijckaert H, Swieten TPV, Driessche IV, Kaczmarek MK, Meijerink A, (2021) High temperature (nano) thermometers based on $LiLuF_4$:Er^{3+}, Yb^{3+} nano- and microcrystals confounded results for core–shell nanocrystals. J Mater Chem C 9:3589–3600
39. Yun X, Zhou J, Zhu Y, Li X, Xu D (2021) Up-conversion luminescence and optical temperature sensing properties of Ho^{3+}-doped double-tungstate $LiYb(WO_4)_2$ J Mater Sci Mater Electron 32:17990–18001
40. Wu X, Lin J, Chen P, Liu C, Lin M, Lin C, Luo L, Zheng X (2019) Ho^{3+}-doped (K,Na)NbO_3-based multifunctional transparent ceramics with superior optical temperature sensing performance. J Am Ceram Soc 102:1249–1258
41. Savchuk OA, Carvajal JJ, Brites CDS, Carlos LD, Aguilo M, Diaz F (2018) Upconversion thermometry: a new tool to measure the thermal resistance of nanoparticles. Nanoscale 10:6602–6610

Figures

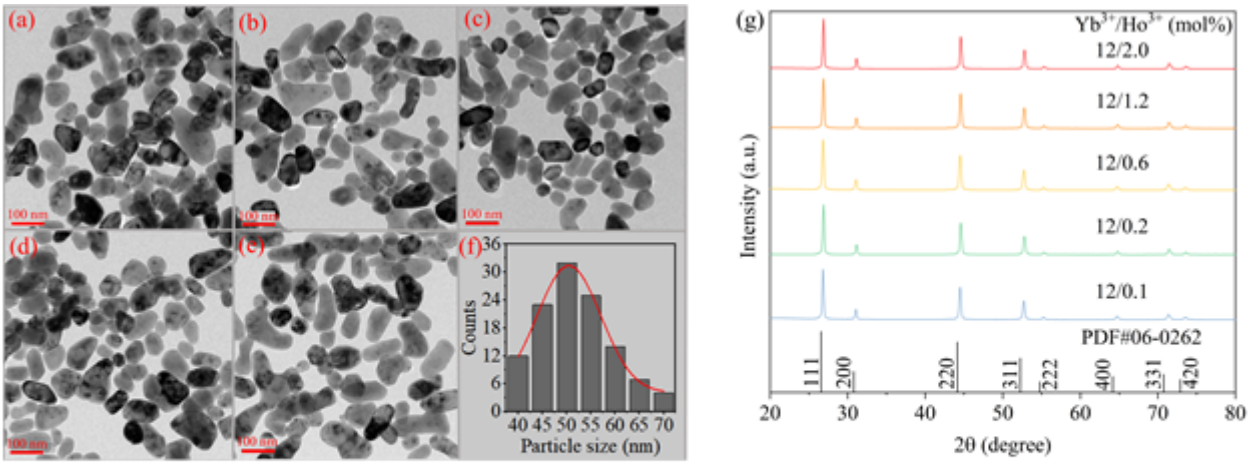

Fig. 1. TEM images of SrF_2:Yb^{3+}/Ho^{3+}(12/x mol%) NCs, (a) x=0.1, (b) x=0.2, (c) x=0.6, (d) x=1.2, (e) x=2.0. (f) The particle size distribution of SrF_2:Yb^{3+}/Ho^{3+} (12/0.1 mol%) NCs. (g) XRD patterns of SrF_2:Yb^{3+}/Ho^{3+} (12/x mol%) NCs doped with different Ho^{3+} concentrations.

Figure 1

See image above for figure legend.

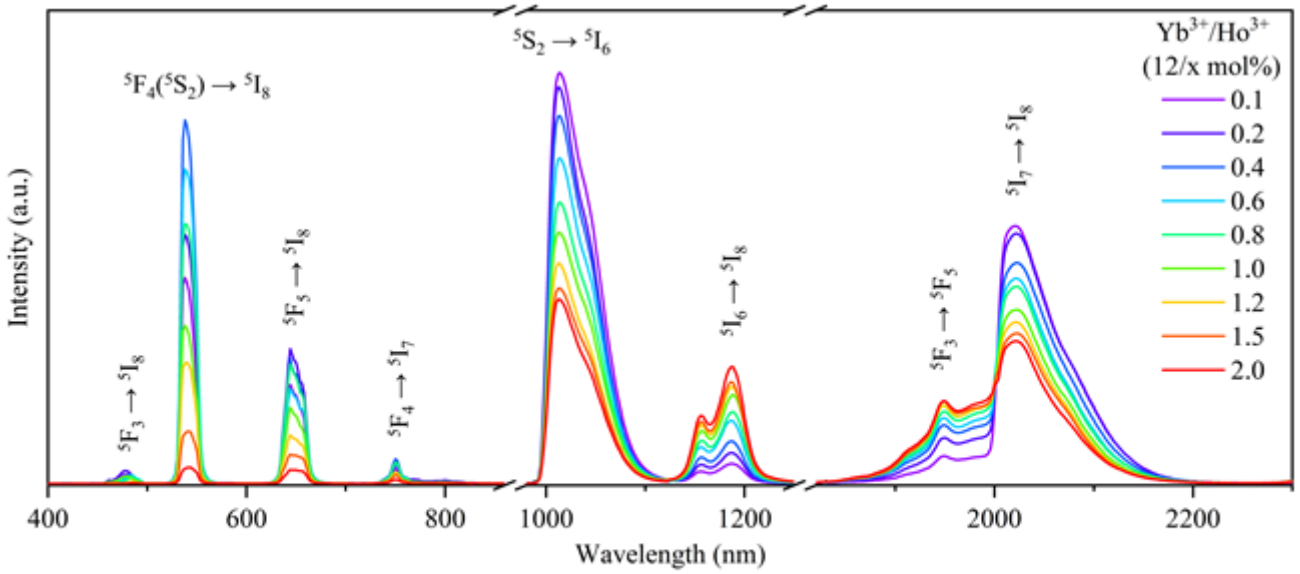

Fig. 2. The visible UCL and NIR DCL spectra of $SrF_2:Yb^{3+}/Ho^{3+}$ (12/x mol%) NCs doped with different Ho^{3+} concentrations under the excitation of 980 nm CW laser.

Figure 2

See image above for figure legend.

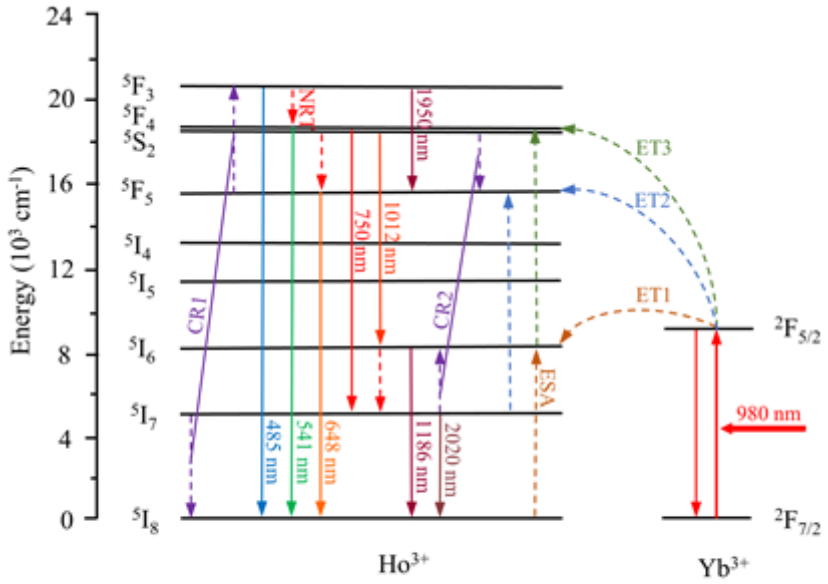

Fig. 3. The energy level diagram for $SrF_2:Yb^{3+}/Ho^{3+}$ NCs excited at 980 nm. The corresponding processes of ET, ESA, CR and NRT are also provided.

Figure 3

See image above for figure legend.

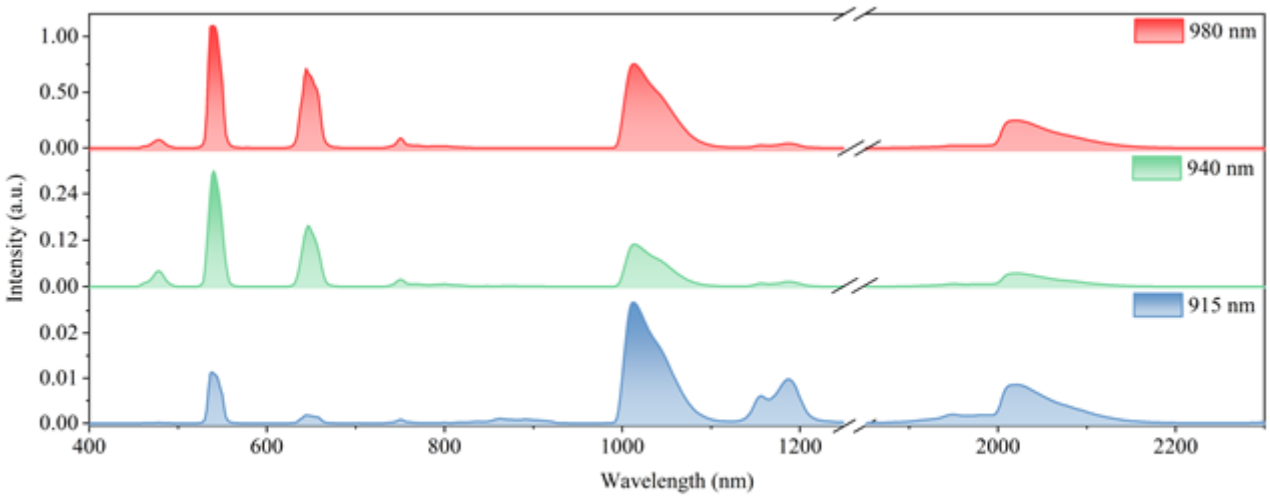

Fig. 4. The spectra of SrF_2:Yb^{3+}/Ho^{3+} (12/0.1 mol%) NCs under the 980, 940 and 915 nm excitations, respectively.

Figure 4

See image above for figure legend.

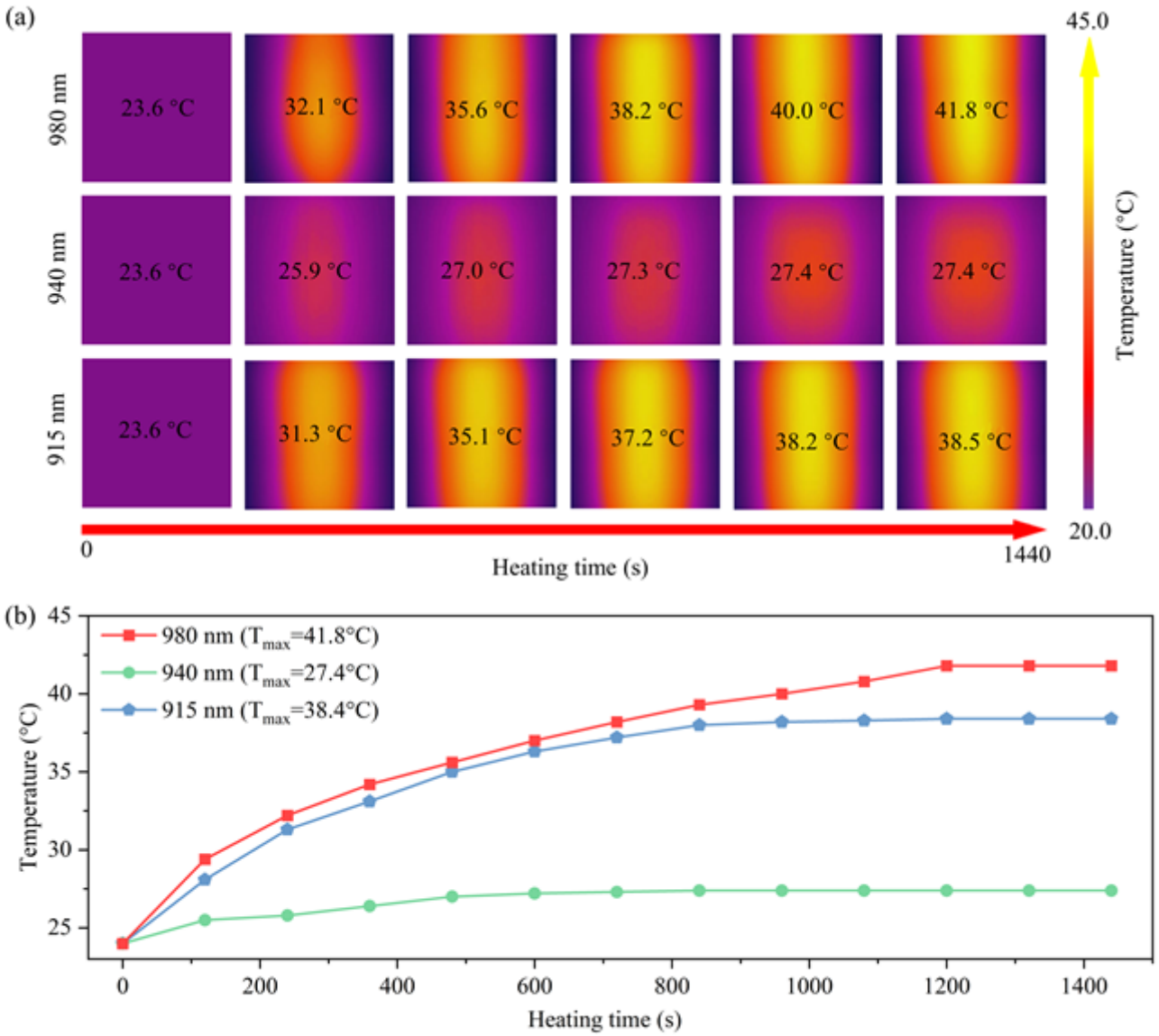

Fig. 5. (a) The thermal images and (b) the relationship between temperature and heating time of $SrF_2:Yb^{3+}/Ho^{3+}$ (12/0.1 mol%) NCs under the 980, 940 and 915 nm excitations, respectively.

Figure 5

See image above for figure legend.

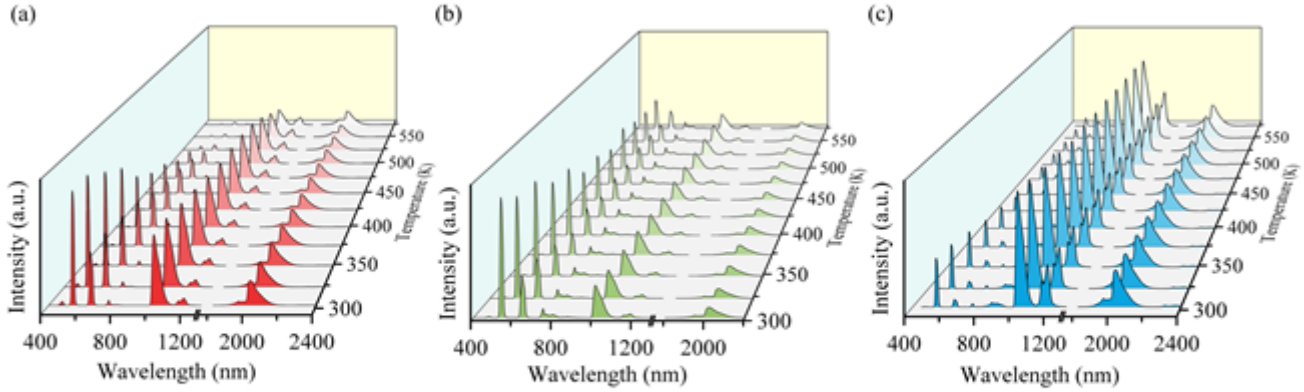

Fig. 6. Temperature-dependent spectra of $SrF_2:Yb^{3+}/Ho^{3+}$ (12/0.1 mol%) NCs under the (a) 980 nm, (b) 940 nm and (c) 915 nm excitations, respectively.

Figure 6

See image above for figure legend.

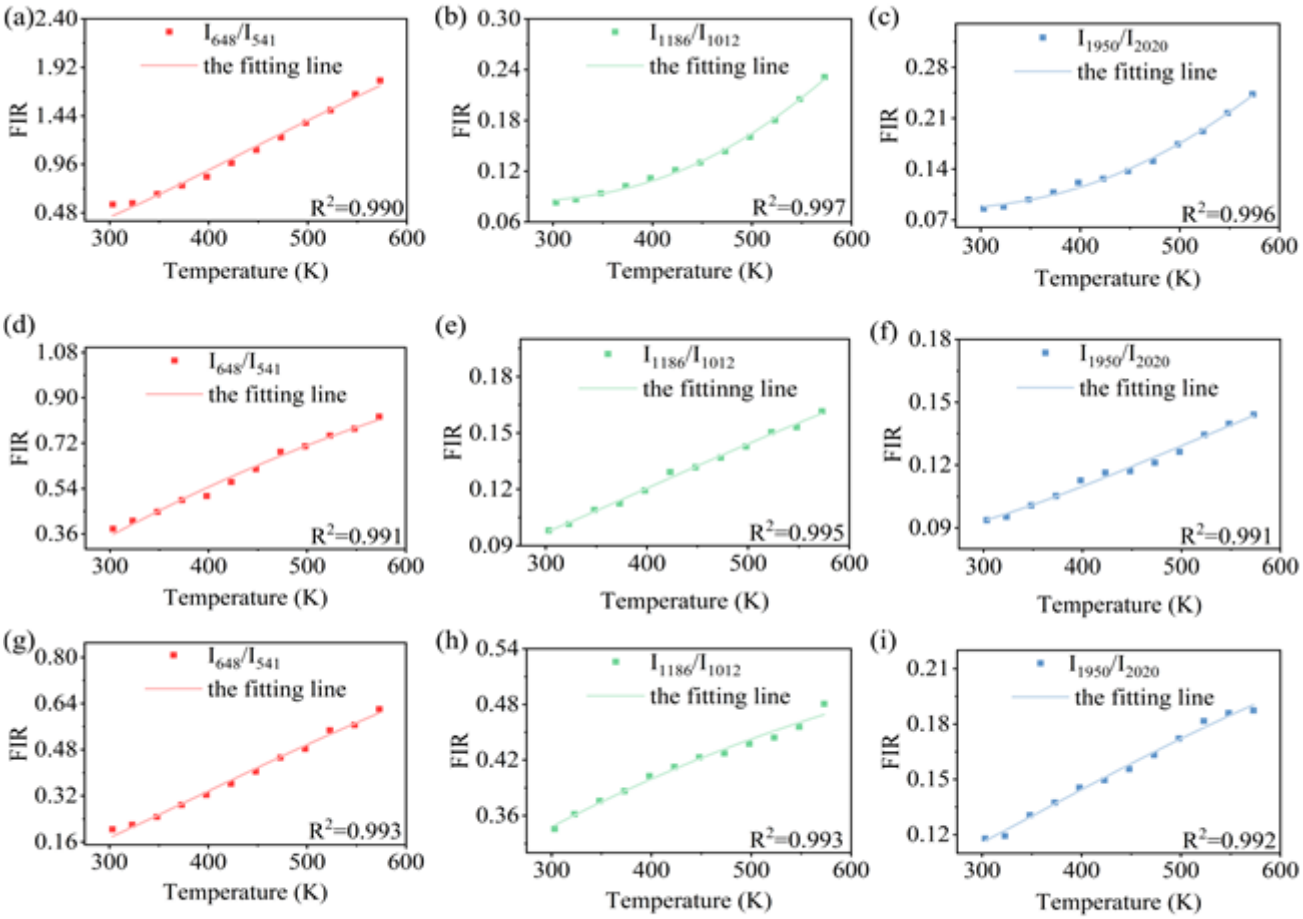

Fig.7. The experimental data (dot) and fitting curves (line) of different FIRs versus temperature of $SrF_2:Yb^{3+}/Ho^{3+}$ (12/0.1 mol%) NCs under the (a-c) 980 nm, (d-f) 940 nm and (g-i) 915 nm excitations, respectively.

Figure 7

See image above for figure legend.

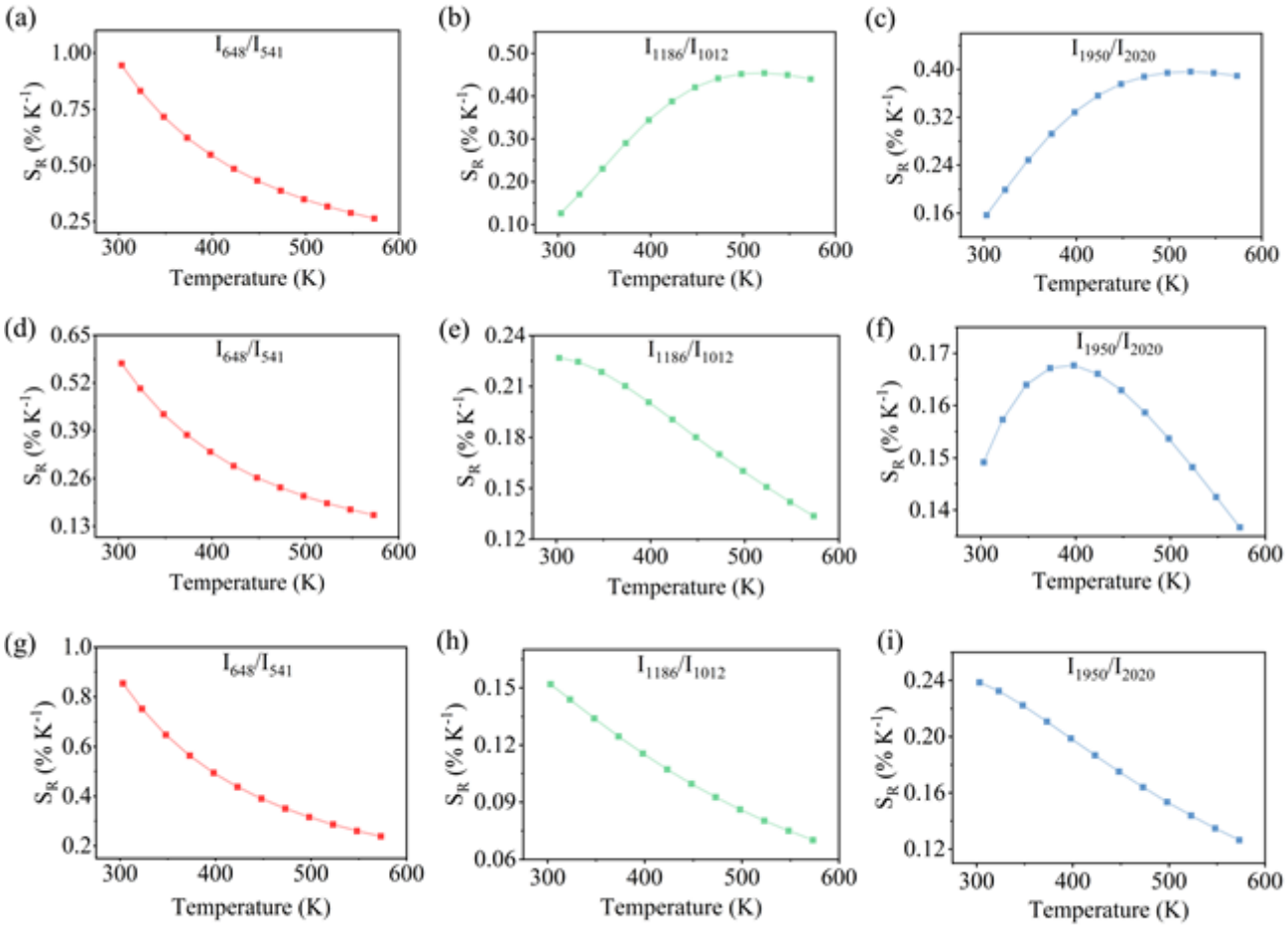

Fig. 8. The relative sensitivity S_R versus temperature of SrF_2:Yb^{3+}/Ho^{3+} (12/0.1 mol%) NCs under the excitation of (a-c) 980 nm, (d-f) 940 nm and (g-i) 915 nm, respectively.

Figure 8

See image above for figure legend.

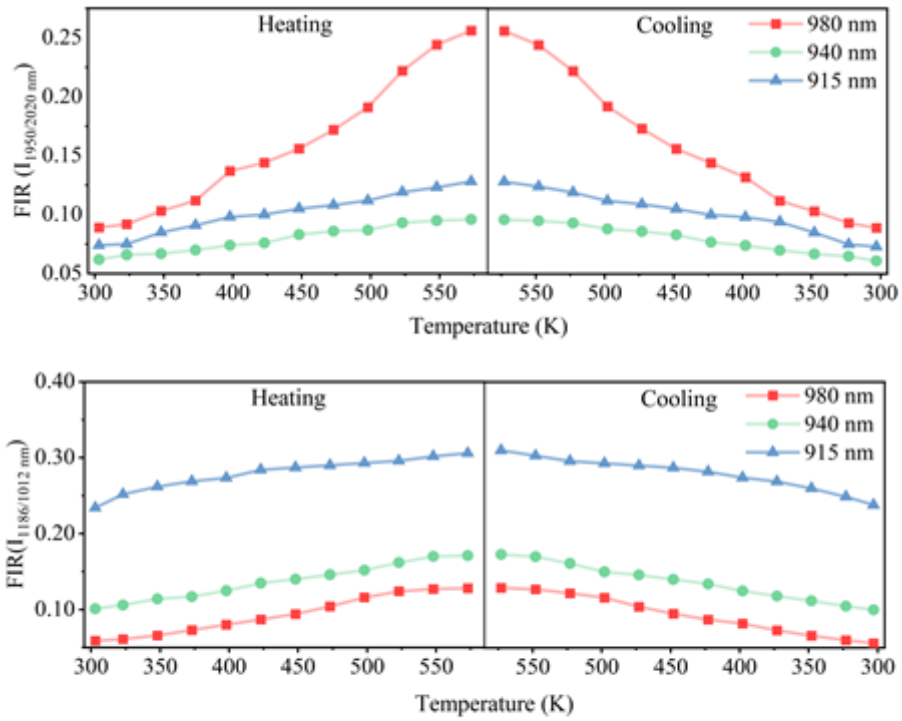

Fig. 9. The repeatability of FIR (I_{1186}/I_{1012} and I_{1950}/I_{2020}) in $SrF_2:Yb^{3+}/Ho^{3+}$ (12/0.1 mol%) NCs over an arbitrary heating and cooling circle under 980, 940 and 915 nm excitations.

Figure 9

See image above for figure legend.